ACS Electrochemistry

Open Access
This article is licensed under CC-BY-NC-ND 4.0

pubs.acs.org/electrochem
Article

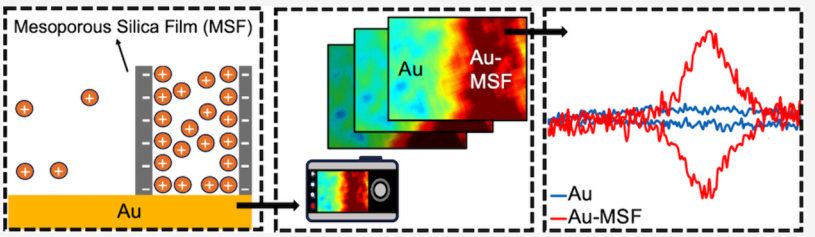
Sensitive Imaging of Electroactive Species in Plasmonic Electrochemical Microscopy Enabled by Nanoconfinement

Samuel Groysman, Yisi Chen, Adaly Garcia, Christian Martinez, Kevin Diego-Perez, Miriam Benavides, Yi Chen, Zijian Wan, Shaopeng Wang, Rujia Liu, Dengchao Wang, Chong Liu,* and Yixian Wang*

Cite This: ACS Electrochem. 2025, 1, 974−986

Read Online

ACCESS | Metrics & More | Article Recommendations | Supporting Information



ABSTRACT: Spatially resolved sensing is a burgeoning area of electrochemistry that, in contrast to traditional electrochemical techniques, allows for the analysis of heterogeneous systems such as neurotransmitter release from cells. Of these techniques, optical microscopy methods are valued for real-time high throughput sensing. However, improving the sensitivity of many optical techniques remains a challenge. Here, we modify the gold (Au) electrode of the standard plasmonic electrochemical microscopy (PEM) setup with a mesoporous silica film (MSF) to achieve sensitive imaging of the electroactive species. Sensitivity enhancement occurs via species nanoconfinement from the attraction of ions to the negatively charged silica films, thereby increasing the local concentration change and magnifying the PEM signal. The performance of Au-MSF electrodes in the PEM setup was investigated using 1,1′-ferrocenedimethanol, whose oxidized form carries a positive charge. Results revealed enhancement of the sensing signal, with up to 37-fold improvement in the detection limit and up to 23 times improvement in the sensitivity. Importantly, Au-MSF electrodes allowed for the quantification of detected concentrations, in contrast to Au electrodes, for which R^2 values were unacceptably low. Furthermore, Au-MSF electrodes also showed increased sensitivity for dopamine detection compared to Au electrodes and were able to visualize localized dopamine release, showing this setup's great promise for biological applications, such as real-time imaging of the neurotransmitter release.

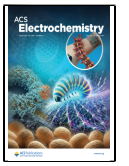
KEYWORDS: *Mesoporous silica films, electrochemistry, surface plasmon resonance imaging, numerical simulation, dopamine detection*

Downloaded via CALIFORNIA STATE UNIV LOS ANGELES on June 18, 2025 at 23:30:29 (UTC).
See https://pubs.acs.org/sharingguidelines for options on how to legitimately share published articles.

INTRODUCTION

Achieving spatially resolved sensing is essential due to the fundamental heterogeneity of all systems. Sensors based on traditional electrochemical techniques provide accurate, real-time measurements of changes in the current at the working electrode surface, but they lack the spatial resolution necessary to investigate its heterogeneous response. Many techniques have been developed to address the lack of spatial resolution provided by traditional electrochemical methods. These include direct current measurement techniques such as microelectrode arrays, scanning electrochemical microscopy, and scanning electrochemical cell microscopy, all of which are able to map the sample surface with micrometer or nanometer resolution.[1−3] Additionally, optical imaging techniques serve as a great alternative in this field, including single-molecule fluorescence microscopy, Raman spectroscopy, and plasmonic electrochemical microscopy.[4−6] Scanning probe-based electrochemical techniques benefit from high spatial resolution but are time-consuming and lack throughput, while optical methods typically have high throughput and temporal resolution at the price of diffraction-limited spatial resolution.[7] Of these techniques, plasmonic electrochemical microscopy (PEM) uses planar surface plasmon resonance (SPR) to spatially resolve refractive index changes induced by electrochemical reactions.[8,9] In contrast to other optical techniques, such as single-molecule fluorescence microscopy,[10] PEM is label free, enabling the native imaging of samples without the need for external markers. By virtue of building upon SPR, PEM has diffraction-limited resolution and provides nanometer precision in the *z*-direction.[11,12] This is essential to accurately characterizing heterogeneous systems. However, PEM typically requires concentrations at the millimolar level or

Received: December 19, 2024
Revised: February 3, 2025
Accepted: February 6, 2025
Published: February 17, 2025



© 2025 The Authors. Published by American Chemical Society

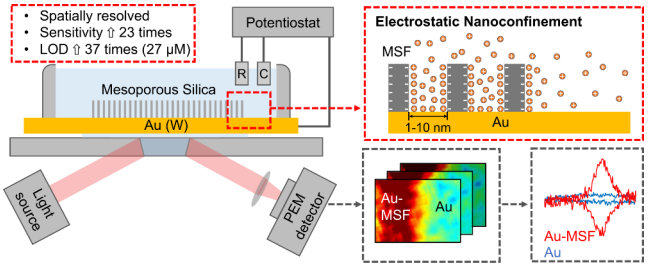
higher.[8,13,14] This requirement arises from a poor signal-to-noise ratio at individual pixels and limited refractive index changes associated with some redox reactions. As a result, the applicability of a standard PEM setup is severely limited since many applications, such as spatially resolving cellular exocytosis, involve the detection of micromolar or sub-micromolar concentrations.[15−17]

One possibility to increase the sensitivity of electrochemical imaging techniques is the modification of the electrode surface. Nanopore electrode arrays have been widely used for spatially resolved sensing and can offer tunable properties depending on the analyte under investigation.[18−20] Mesoporous silica films (MSFs) are arrays of nano-sized pores typically 1 to 3 nm in diameter and 50 to 400 nm in height.[21] MSFs and mesoporous silica nanoparticles have been utilized for applications including sensing, energy storage, and drug delivery.[22−25] Previous work has shown that MSFs can enhance the sensitivity of the SPR signal due to the nanoconfinement of select chemicals on the negatively charged pore walls, which have a high surface area.[26−30] Similarly, MSFs were also shown to enhance the electrochemical signal arising from the oxidation and reduction of paraquat, a positively charged pesticide.[31] However, to the best of our knowledge, MSFs have yet to be utilized in an optical imaging setup for spatially resolved sensing of electrochemically active species.

Herein, we introduce electrostatic nanoconfinement facilitated by mesoporous silica films to PEM, enabling the sensitive imaging of electroactive species (Scheme 1). In this setup, the gold (Au) electrode, serving as both the PEM sensor and the working electrode, was coated with a mesoporous silica film through electrochemically assisted self-assembly (EASA), forming Au-MSF electrodes.[32] The potentiostat controls the electrochemical processes through the three-electrode system, while the PEM objective simultaneously monitors the optical signal changes associated with these processes, generating sequences of images. The raw signal can be extracted from the plasmonic images (denoted as PEM signal, with units of %) and can be differentiated with respect to time (denoted as dPEM/dt signal, with units of %/s)) to better capture dynamic changes in PEM signal during electrochemical measurements.

The signal enhancement phenomenon is hypothesized to occur as a result of the electrostatic nanoconfinement of ions within the charged pore, thereby leading to a greater concentration change and, hence, a greater optical signal. We observed profound enhancement of the PEM signal of a model redox species, 1,1′-ferrocenedimethanol (FC), with a positively charged oxidized form, 1,1′-ferroceniumdimethanol (FC^+), when nanoconfinement was incorporated: linear response for micromolar concentrations as well as approximately 37-fold improvement in the detection limit and 23 times improvement in the sensitivity compared to a standard PEM setup without nanoconfinement. The new technique was also able to visualize the local delivery of dopamine from a micropipette, demonstrating its potential in biological applications, such as real-time imaging of neurotransmitter release. Additionally, we introduced customized gridded gold electrodes that allow for retracing imaging locations and demonstrated their sensing capabilities.

Scheme 1. Electrostatic Nanoconfinement Facilitated by a Mesoporous Silica Film (MSF), Enabling Sensitive Imaging of a Model Electroactive Species in the Plasmonic Electrochemical Microscopy (PEM) Setup[a]

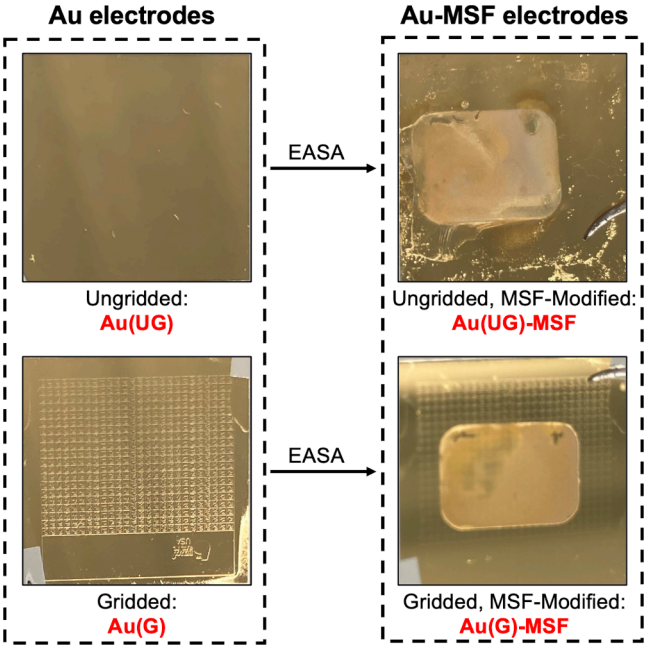


[a]The PEM setup comprises a Au working electrode (W), counter electrode (C), reference electrode (R), light source, and detector. The sensitivity and limit of detection (LOD) are compared to a standard PEM system without nanoconfinement. The imaging feature directly reveals the enhancement of PEM signal by Au-MSF electrodes.

RESULTS AND DISCUSSION

Real-Time Monitoring of Mesoporous Silica Film Deposition and Characterization. Scheme 2 illustrates the visual differences between the Au electrodes and the Au-MSF electrodes. Two types of gold electrodes were used in the experiments: ungridded gold (denoted as Au(UG)) and gridded gold (denoted as Au(G)). Depositing an MSF onto these electrodes results in Au(UG)-MSF and Au(G)-MSF, respectively. Gridded electrodes were preferred due to the presence of labels on the electrode surface, which facilitated easier identification and analysis. As a result, most of the working electrodes referenced in the main text were gridded, though ungridded electrodes were also examined for comparison.

Scheme 2. Different Electrodes Used in PEM Experiments



The deposition of an MSF was monitored both electrochemically and optically. A Au(G) electrode was selected for its ability to facilitate the identification of the same sensing area across different experiments. Before deposition, a raw bright-field image was captured (Figure 1A). MSF synthesis was performed following reported procedures.[32] The deposition

https://doi.org/10.1021/acselectrochem.4c00227
ACS Electrochem. 2025, 1, 974−986

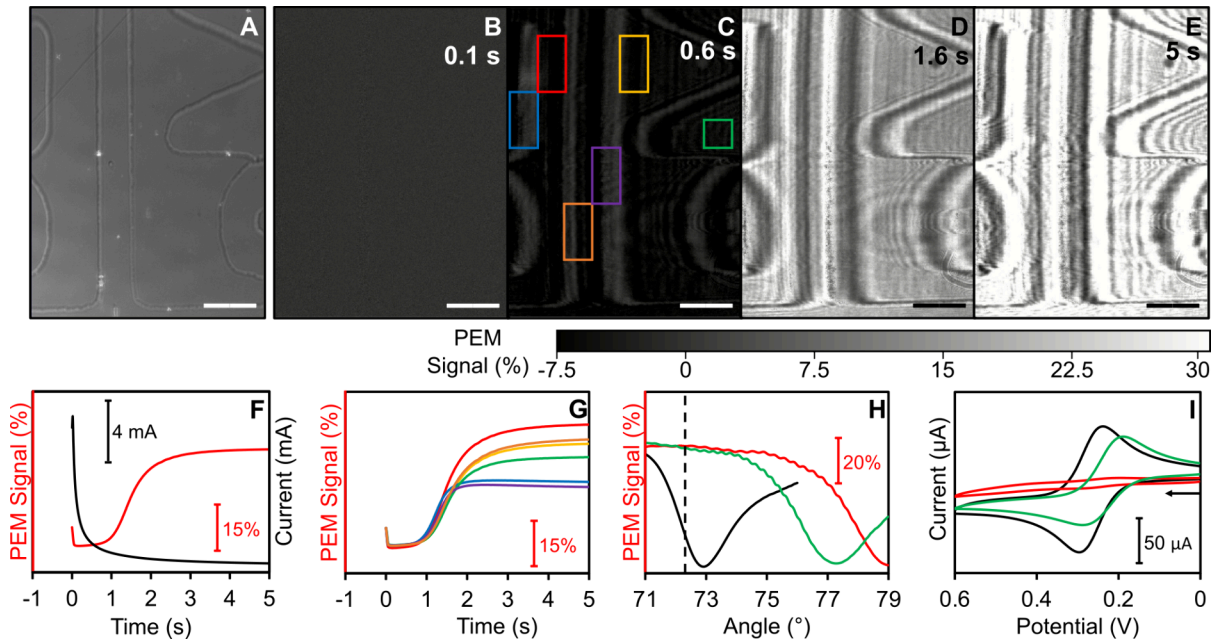


Figure 1. Real-time deposition of an MSF. A, Bright field image of a Au(G) electrode before deposition (scale bar, 100 μm). B-E, PEM images of the same area as (A) following background subtraction of the first deposition frame at 0.1 seconds (B), 0.6 seconds (C), 1.6 seconds (D), and 5 seconds (E) into the deposition process (scale bar, 100 μm). F, Real-time averaged PEM signal (%, red) and current (mA, black) during the 5 second deposition. G, Real-time PEM signal from the regions boxed in (C) over the 5 second deposition. H, PEM angle sweeps of the same area before deposition (black), after deposition but before surfactant removal (red), and after surfactant removal (green). The dotted line represents the incident angle used for imaging only during the deposition. I, Cyclic voltammograms of the Au(G) electrode (black) and the Au(G)-MSF electrode before surfactant removal (red) and after surfactant removal (green). The starting potential is 0 V, the scan rate is 0.10 V/s, and the analyte is an aqueous solution of 500 μM FC and 0.1 M $NaNO_3$.

solution was prepared by combining 100 mM tetraethoxysilane, 32 mM cetyltrimethylammonium bromide, and 0.1 M $NaNO_3$ in a 1:1 (v/v) water/ethanol solution. The Au(G) electrode was pretreated with 0.1 mM (3-mercaptopropyl)-trimethoxysilane. Deposition was carried out at a potential of -1.2 V for 5 s, during which plasmonic images were simultaneously recorded (Figures 1B-1E). All images were background-subtracted with the first deposition frame. Initially, the intensity of the plasmonic signal decreased, likely due to the double layer charging caused by the applied negative potential (Figures 1B, C). Thereafter, the plasmonic signal intensity increased as cationic surfactant hemimicelles assembled on the surface of the Au(G) electrode, forming vertically growing films (Figures 1D, E).[33] To further analyze the deposition process, we extracted the average plasmonic signal (red) from the sensing area and correlated it to the electrochemical signal (black) from the entire electrode surface over the course of the deposition (Figure 1F). Unlike traditional electrochemical techniques, the spatial resolution provided by PEM allows for a detailed comparison of signal intensity changes across different parts of the substrate. Figure 1G displays the PEM signals over deposition from the areas marked with colored boxes in Figure 1C. This disparity in signal increase (ranging from 14% to 26%) is due to the heterogeneous nature of the Au(G) electrode and can be mitigated if desired (see the section titled "Comparing Gridded and Ungridded Gold Electrodes"). Interestingly, all plasmonic deposition profiles exhibit a plateauing of the PEM signal at around the 2 s mark of the deposition. This is likely due to the deposition process slowing down and the plasmonic signal saturating due to a significant PEM resonance angle change during the deposition, as indicated by the red and black curves in Figure 1H.

As expected for a modification of the PEM electrode, there is a 6.1° increase in the resonance angle after deposition with a moderate 1.7° decrease in the angle after surfactant removal (Figure 1H). The dotted line represents the incident angle at which the deposition process was imaged. The angle was changed for subsequent experiments, with the exact value depending on the angle sweep of the area being imaged. Cyclic voltammograms (CVs) from various stages of the deposition process align with literature predictions (Figure 1I).[32] The angle sweep and recorded CVs are similar to those from a Au(UG) electrode (Figure S1).

Characterization by scanning electron microscopy (SEM) and energy-dispersive x-ray spectroscopy (EDX) further confirmed the deposition and uniformity of the mesoporous silica films, showing some aggregation due to hydroxide radical generation beyond the electrode surface,[33] with EDX indicating nearly complete surface coverage by silicon and oxygen from silanol groups (Figures S2A-D). Atomic force microscopy (AFM) images revealed an MSF thickness of 60 ± 11 nm and increased surface roughness (8 ± 1 nm) compared to bare gold (1 nm), consistent with literature values (Figures S2E-H).[21]

Visualization of Signal Enhancement along a Au/Au-MSF Boundary. A boundary between the Au-MSF region and the Au region (Figure 2A) was tested to directly investigate the effect of signal enhancement.

We monitored the change in the current (Figure 2B) and PEM signal intensity (Figure 2C) while performing CV using 250 μM FC. Strikingly, we observed greater PEM signal change in the red Au-MSF region compared with the blue Au

https://doi.org/10.1021/acselectrochem.4c00227
ACS Electrochem. 2025, 1, 974−986

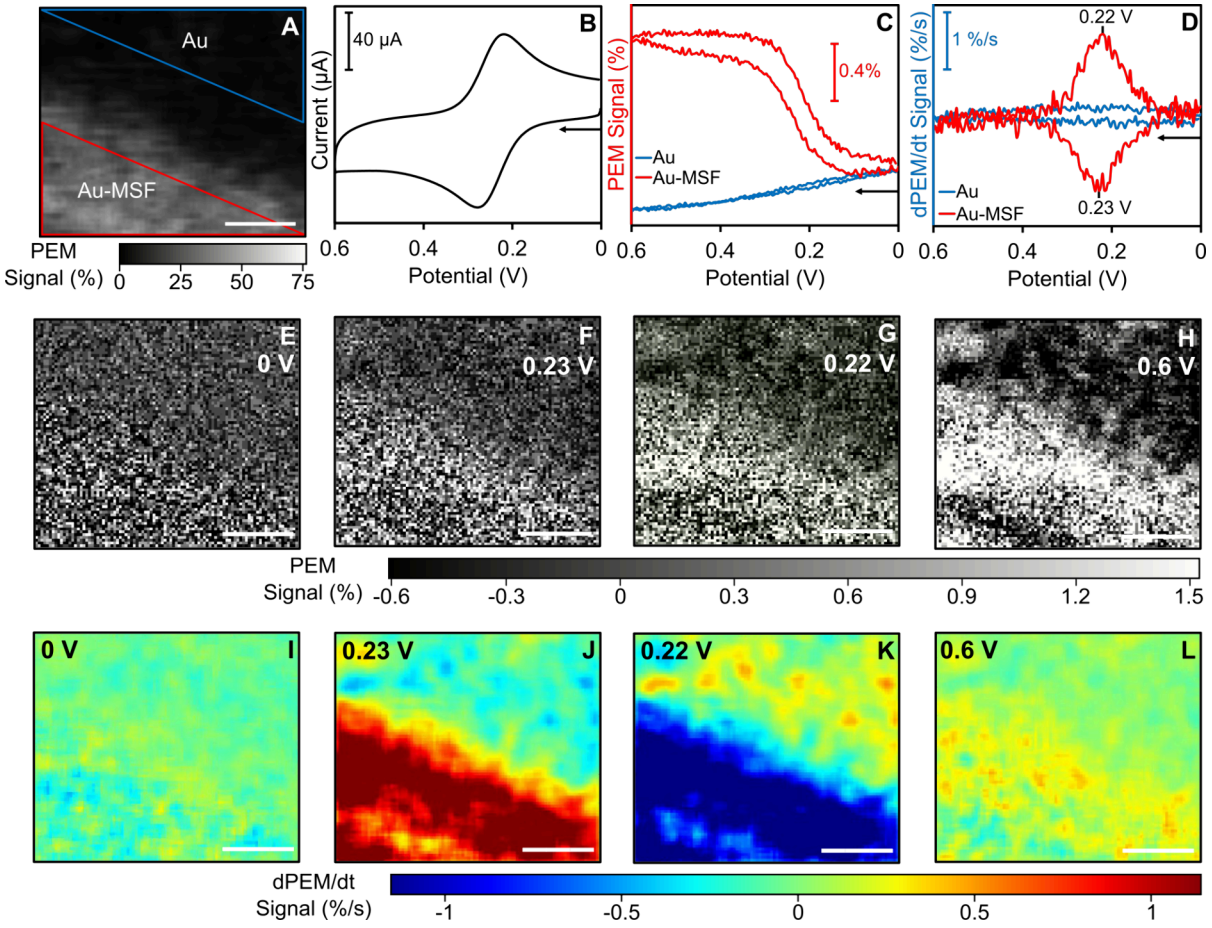


Figure 2. PEM signal along a Au/Au-MSF boundary. A, Raw PEM image of a Au/Au-MSF boundary. B, CV of the entire working electrode surface. C, Comparison of the raw PEM signal in the Au-MSF region (red) and the Au region (blue) in (A). D, Comparison of the time derivative of the PEM signal in the Au-MSF region (red) and the Au region (blue) in (A). E-H, Background-subtracted PEM signal at the starting potential (E), oxidation peak potential (F), reduction peak potential (G), and vertex potential (H). I-L, Time derivative of PEM intensity data from the same area in (A) at the starting potential (I), oxidation peak potential (J), reduction peak potential (K), and vertex potential (L). Deposition was performed at -0.8 V for 5 seconds. For all graphs, the starting potential is 0 V, the scan rate is 0.20 V/s, the electrolyte solution is 0.1 M $NaNO_3$, and the analyte is 250 μM FC. All scale bars are 20 μm.

region (Figure 2C). While the PEM signal for the Au region displays typical charging and discharging behavior, the Au-MSF region displays a clear increase near the standard reduction potential of FC (~0.2 V). This difference is also apparent in the dPEM/dt signal plot from each region (Figure 2D). Since PEM is a microscopy-based technique, we were also able to acquire images of the raw PEM signal of the region. As with the average extracted signal, we observed a greater signal change in the MSF region compared to the Au region at the peak dPEM/dt oxidation potential of 0.23 V, the peak dPEM/dt reduction potential of 0.22 V, and the vertex potential of 0.6 V, but not the starting potential of 0 V (Figures 2E-H). A similar trend existed in the dPEM/dt images (Figures 2I-L), with a notable difference being that the vertex potential does not show a clear difference in signal intensity due to the reaction reaching steady-state conditions. Notably, these spatial signal differences are not detectable with traditional voltammetric techniques, which provide only the average signal for the entire sensing surface.

Interestingly, the dPEM/dt signal plot exhibits a peak separation of approximately 0 V, suggesting a surface redox process. This is likely due to PEM's enhanced sensitivity for reactions occurring near the sensing surface, making it particularly responsive to adsorption of the oxidized form FC^+ onto the MSF, the proposed mechanism for signal enhancement (see the section "Investigating the Mechanism of Signal Enhancement"). As a comparison, we tested a diffusion-controlled system, 10 mM potassium ferricyanide with a Au electrode, and observed peak separation in the dPEM/dt signal (Figure S3). It should be noted that the dPEM/dt signal was not intended as an approximation for the current as it does not accurately model processes with a diffusion-limited component, as reflected by the CV (Figure 2B). Rather, the dPEM/dt signal was used to highlight the change in the PEM signal over time. Accurately converting the optical signal to current requires knowledge of the changes in the local refractive index per unit concentration for the oxidized and reduced molecules, which proved difficult to acquire due to signal stabilization issues with the oxidized species.

Directly imaging additional surfaces containing a boundary between Au and Au-MSF regions has been challenging due to the formation of residues at the edge, which makes it difficult to achieve a clean boundary. Additionally, the significant difference in resonance angles between Au and Au-MSF regions complicates simultaneous imaging of both areas. However, a consistent signal difference was observed between

https://doi.org/10.1021/acselectrochem.4c00227
ACS Electrochem. 2025, 1, 974−986

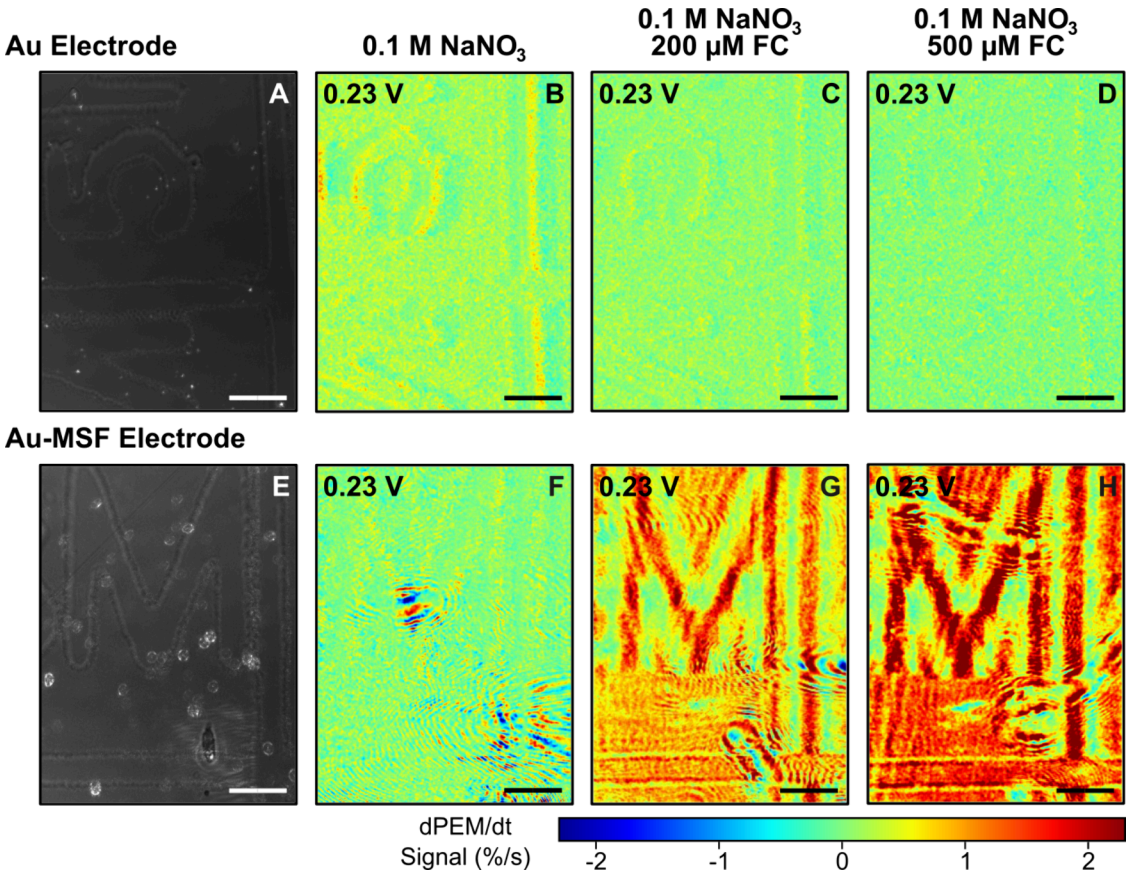


Figure 3. Plasmonic imaging of Au(G) and Au(G)-MSF electrodes with FC additions. A-D, PEM data from a Au(G)-MSF electrode including the bright field image at 0 V (A) and dPEM/dt images at the oxidation peak potential (0.23 V according to the plasmonic CV in Figure 2D) for 0.1 M $NaNO_3$ alone (B) and with 200 μM FC (C) or 500 μM FC (D) added. E-H, PEM data from a Au(G)-MSF electrode including the bright field image at 0 V (E) and dPEM/dt images at the oxidation peak potential for 0.1 M $NaNO_3$ alone (F) and with 200 μM FC (G) or 500 μM FC (H) added. For all electrochemical measurements, the scan rate is 0.10 V/s and the electrolyte solution is 0.1 M $NaNO_3$. All scale bars are 100 μm.

individual Au and Au-MSF electrodes across multiple experiments. Specifically, at least 4 Au and 8 Au-MSF electrodes were tested, and in all cases, the Au-MSF electrodes exhibited a greater signal.

Quantitative Measurement Using Au-MSF Electrodes. To further evaluate and quantify the enhanced sensing capabilities of this new technique, we investigated the concentration dependence of the PEM signal before and after MSF deposition. The concentration dependence was tested by analyzing the PEM signal with increasing concentrations of FC added to a 0.1 M $NaNO_3$ electrolyte. For the Au(G) electrode (Figures 3A), the dPEM/dt signal from the electrolyte only (Figure 3B) was slightly greater than the signal from FC additions (Figures 3C and D), but little difference was observed between the two FC concentrations. In contrast, Figures 3E-H represents results from the Au(G)-MSF electrode, which demonstrates a clear concentration-dependent increase in the dPEM/dt signal. The white dots and disks in the bright field images (Figures 3A and 3E) are likely impurities or defects on the Au(G) electrode.

The dPEM/dt signals were extracted and plotted against the applied voltage for both the electrolyte-only condition and varying FC concentrations in Figure 4. As observed previously, the Au(G) electrode did not show a clear linear concentration dependence (Figures 4A), whereas the Au(G)-MSF electrode showed a clear concentration-dependent signal increase across two concentration ranges (Figure 4B and Figure 4C). The calibration curves plotted using peak dPEM/dt values further illustrate this trend. The Au(G) electrode displayed little correlation and large standard deviations (Figures 4D), demonstrating that the standard PEM setup lacks sufficient sensitivity to detect concentration changes associated with the transition between FC and FC^+. In contrast, the calibration curves from the Au(G)-MSF electrode demonstrated high accuracy, achieving an R^2 value of 0.95 for the 100 to 500 μM range (Figure 4E) and an R^2 value of 0.92 for the 10 to 50 μM range (Figure 4F). The difference in slope/sensitivity between these two concentration ranges is due to measurements being performed in different regions of the Au(G)-MSF electrode. This further highlights the necessity of using a spatially resolved sensing technique to perform calibration at the micrometer level.

Within the 10-50 μM range, the Au(G)-MSF electrode achieved a limit of detection of 27 μM for the anodic current and 35 μM for the cathodic current, representing an improvement of up to 37 times compared to the Au(G) electrode (Figures 4D and 4F, Table 1). The sensitivity was also improved by up to 23 times (Figures 4D and 4F, Table 1). More importantly, although we used the slope from the Au(G) electrode calibration curve to calculate the limit of detection, the R^2 values were unacceptably low. This demonstrates that the Au(G)-MSF electrode enables quantifiable detection of the signal, whereas the Au(G) electrode does not provide reliable quantification. Signal enhancement associated with MSF

https://doi.org/10.1021/acselectrochem.4c00227
ACS Electrochem. 2025, 1, 974−986

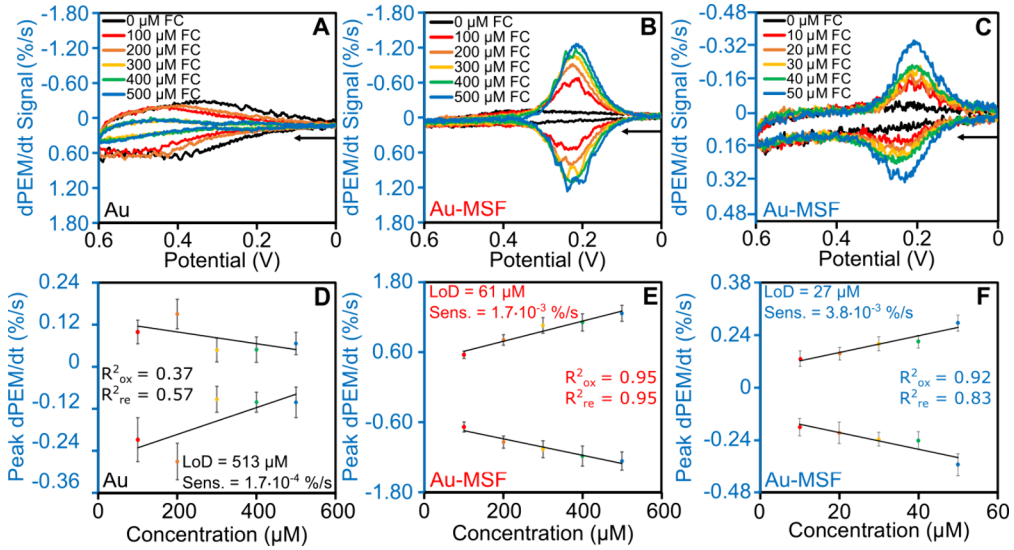


Figure 4. Comparing the concentration dependence of plasmonic signals for Au(G) and Au(G)-MSF electrodes. A, Extracted dPEM/dt signal from the Au(G) electrode tested in Figures 3A-D. B, Extracted dPEM/dt signal from the Au(G)-MSF electrode tested in Figures 3E-H. C, Extracted dPEM/dt signal from the Au(G)-MSF electrode at lower concentrations. D-F, Calibration curves for the anodic and cathodic sweeps of the dPEM/dt graphs in parts A (D), B (E), and C (F). For all electrochemical measurements, the starting potential is 0 V, the scan rate is 0.10 V/s, and the electrolyte solution is 0.1 M $NaNO_3$. The analyte used is FC, with concentrations of 100 μM, 200 μM, 300 μM, 400 μM, and 500 μM being denoted by red, orange, yellow, green, and blue curves, respectively, in A and B, and concentrations of 10 μM, 20 μM, 30 μM, 40 μM, and 50 μM being denoted by red, orange, yellow, green, and blue curves, respectively, in C. The black curve represents the electrolyte solution alone. Pearson correlation coefficient (R^2) values were calculated as described in the supplemental methods for the anodic (R_{ox}) and cathodic (R_{re}) sweeps. As supporting information, the CV data, raw PEM signals, and their corresponding calibration curves from electrodes shown in Figures 3 and 4 can be found in Figure S4 and S5.

Table 1. Plasmonic Sensitivity and Limit of Detection of Au and Au-MSF Electrodes

	Limit of Detection (μM)		Sensitivity (%/(μM×s)×10^{-4})	
Setup	Anodic	Cathodic	Anodic	Cathodic
Au(G)	1000	510	1.7	1.7
Au(G)-MSF	28	35	38	38
Au(UG)-MSF	38	51	21	24

deposition may partially arise from the lower signal for the $NaNO_3$ background compared with the Au(G) electrode. The decrease in the background signal is likely a result of a lower charging current for the Au(G)-MSF electrode, arising from a smaller exposed surface area. Other factors contributing to signal enhancement are discussed in the section "Investigating the Mechanism of Signal Enhancement."

One limitation to this setup is that standard deviations for both PEM and dPEM/dt signals are not small (Figures 4F, S5K, and L), which is also apparent in the plotted images. This is likely due to the deposition process not being uniform at a gridded electrode, as observed in Figure 1. Thus, we tested a Au(UG)-MSF electrode to remove the variation introduced by the heterogeneity of the grid (Figure S6). Notably, the recorded plasmonic signals between the two electrodes are quite consistent, with values of around 1.5% and 1.2%/s for the PEM signal and dPEM/dt signal, respectively, for 500 μM FC. As expected, the standard deviation for both PEM and dPEM/dt signals is much lower for the Au(UG)-MSF electrode (Figure S7). However, this did not correspond to a lower limit of detection (Table 1) because the standard deviation for the electrolyte was similar. Moreover, the sensitivity of the Au(UG)-MSF electrode was also similar to that of the Au(G)-MSF electrode (Table 1). This suggests that both Au(UG)-MSF and Au(G)-MSF electrodes enhance the plasmonic signal associated with FC and provide similar sensitivities and limits of detections.

Investigating the Mechanism of Signal Enhancement. We hypothesized that the PEM signal enhancement was caused by electrostatic nanoconfinement, whereby negatively charged mesopores enriched the concentration of the cation FC^+ formed from FC oxidation (Scheme 1). Porous materials have unique mass transfer properties and can potentially trap redox species during an electrochemical experiment, acting as arrays of thin layer cells along the surface of the electrode.[34] To investigate this hypothesis, we probed whether the negative charge of the MSFs is responsible for confining FC^+ and consequently enhancing the PEM signal. We first performed qualitative numerical simulations of Au (Figures 5A and 5B) and Au-MSF electrodes (Figures 5C and 5D) to investigate whether the mesopores can enhance the local concentration of FC^+. The surface charge density of the pore was approximate using literature values,[35] and the simulation monitored a simplified experimental setup wherein 500 μM FC and FC^+ diffused from an inlet at the bottom of the geometry to an outlet at the top of the geometry. As expected, no localized enhancement of FC or FC^+ was observed at the unmodified electrode (Figure 5A,B). However, for the porous model, FC^+ was enriched near the pore wall (Figure 5D), while enhancement of FC was not observed (Figure 5C). Simulation results from varied surface charge densities further supported the hypothesis. At less negative surface charge densities, the concentration of FC was unaffected (Figure 5E), while a much lower concentration of FC^+ within the pore was observed (Figure 5F). Additionally, enhancement is also likely facilitated by nanoscale transport

https://doi.org/10.1021/acselectrochem.4c00227
ACS Electrochem. 2025, 1, 974−986

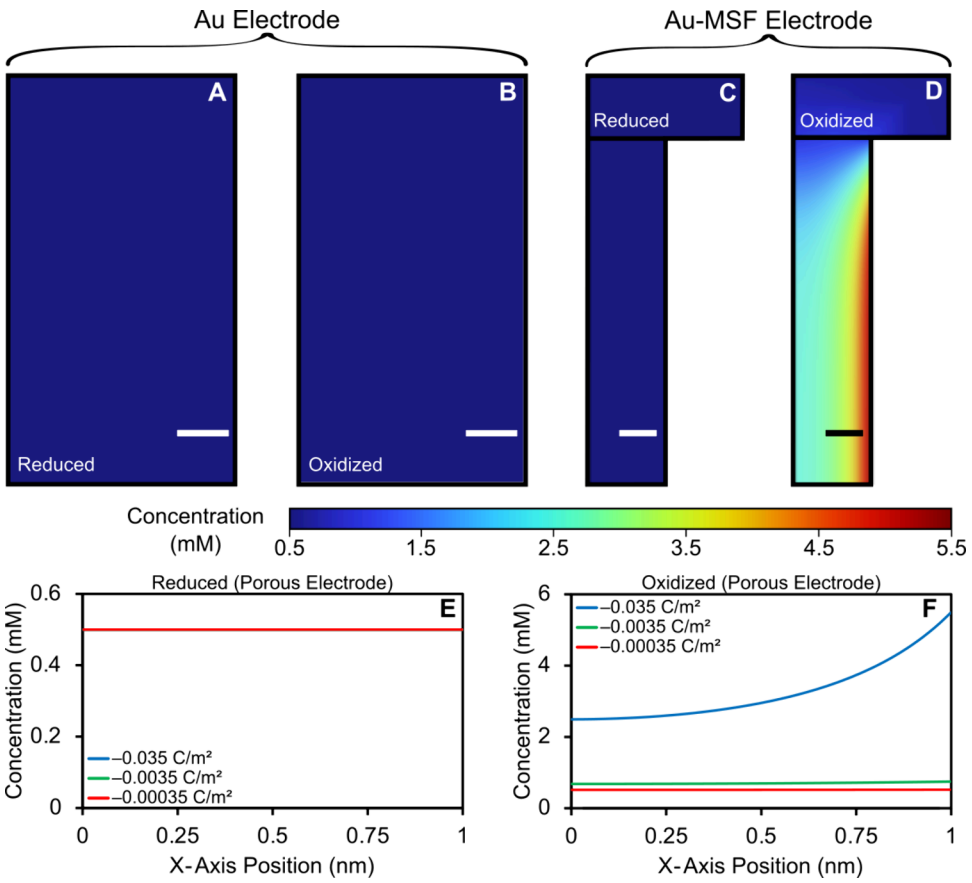


Figure 5. Simulation of FC diffusion. A, B, Concentration distribution of the reduced (A) and oxidized (B) forms of FC at equilibrium in a geometry approximating the Au electrode (scale bars, 0.5 nm). C, D, Concentration distribution of the reduced (C) and oxidized (D) forms of FC at equilibrium in a geometry approximating the Au-MSF electrode (surface charge density = -0.035 C/m^2). Both images are zoomed in near the boundary between the pore and the solution (scale bars, 0.5 nm). E, F, Concentration profiles of the reduced (E) and oxidized (F) forms of FC at equilibrium along the middle of the pore.

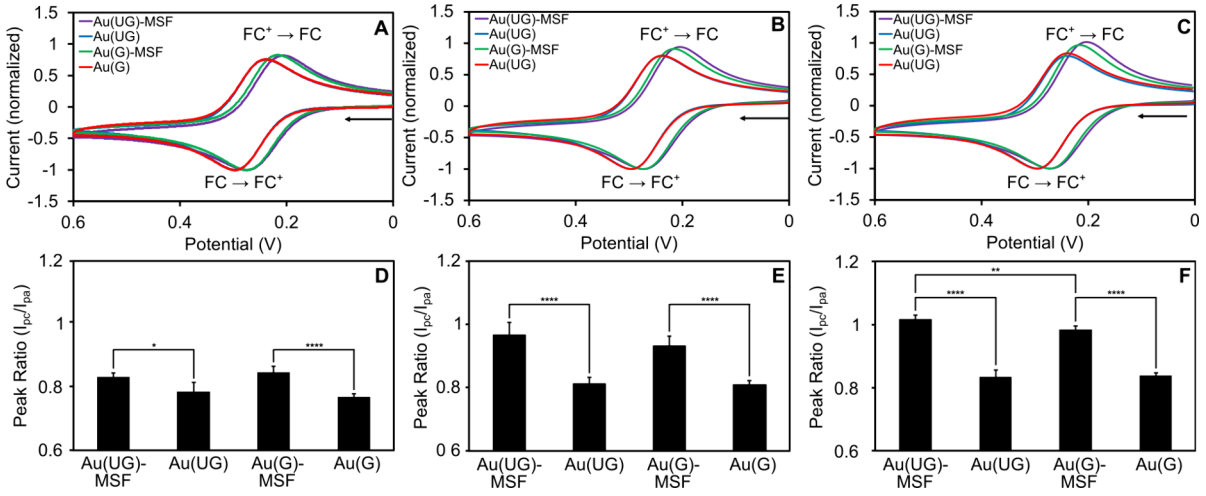


Figure 6. Comparison of normalized cathodic-to-anodic peak ratios for Au and Au-MSF electrodes. A−C, Normalized cyclic voltammograms for 500 μM FC at scan rates of 0.05 V/s (A), 0.10 V/s (B), and 0.20 V/s (C) normalized to the peak anodic current for a Au(UG)-MSF electrode (purple), a Au(UG) electrode (blue), a Au(G)-MSF electrode (green), and a Au(G) electrode (red). D−F, Comparison of the cathodic-to-anodic peak ratio of electrodes at scan rates of 0.05 V/s (D). 0.10 V/s (E), and 0.20 V/s (F); n = 5 for all groups, representing different concentrations tested on the same gold electrode. Error bars represent ± SD (standard deviation). *p<0.05, **p<0.01, ***p<0.001, ****p<0.0001 from one-sided independent t-test. Where not shown, the difference between ungridded and gridded electrodes is not significant.

phenomena that further enrich the concentration of the redox species.[31,36]

With the simulation confirming local enhancement in concentration of FC^+, we revisited the CV data to identify evidence further supporting FC^+ nanoconfinement, especially

https://doi.org/10.1021/acselectrochem.4c00227
ACS Electrochem. 2025, 1, 974−986

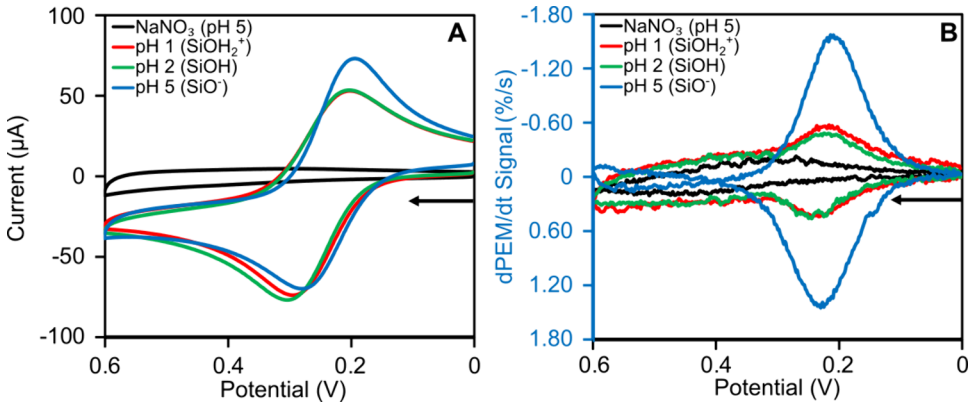


Figure 7. Effect of tuning the MSF surface charge density by adjusting solution pH. A, B, The effect of solution pH on electrochemical (A) and plasmonic (A) signal. For A, B the analyte used is 500 μM FC, with pHs of 1.2, 2.2, and 5 being represented by red, green, and blue curves, respectively. The black curves represent the electrolyte solution alone. For all graphs, the starting potential is 0 V, the scan rate is 0.10 V/s, and the electrolyte solution is 0.1 M $NaNO_3$.

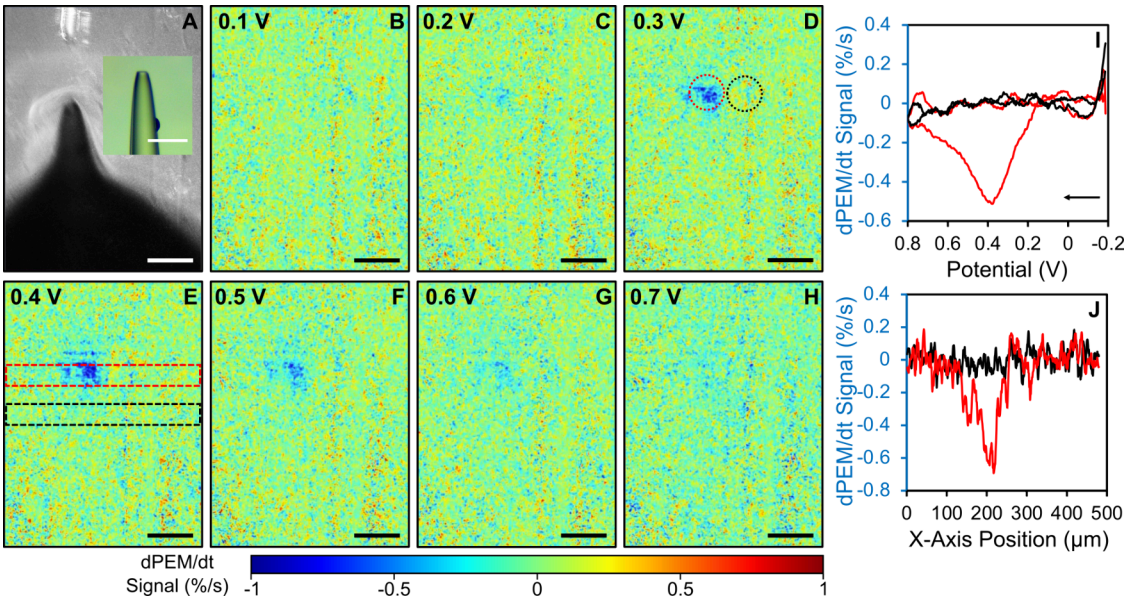


Figure 8. Detecting dopamine locally delivered from a 10 μm micropipette. A, Brightfield image of the micropipette during approach. The inset is an optical image of the pipette prior to use (scale bar, 50 μm). B–H, Images of the dPEM/dt signal at 0.1 V (B), 0.2 V (C), 0.3 V (D), 0.4 V (E), 0.5 V (F), 0.6 V (G), and 0.7 V (H) during the anodic sweep of a cyclic voltammogram with the pipette 3 μm above the sensing surface (scale bars, 100 μm). I, Extracted dPEM/dt signal during the CV for the red and black regions in (D). J, Extracted dPEM/dt signal from the line profiles in (E). For all electrochemical measurements, a quiet time of 20 seconds was used at the starting potential of -0.2 V, the scan rate is 0.20 V/s, the electrolyte solution is 0.1 M $NaNO_3$, and the micropipette was filled with the same electrolyte solution plus 10 mM dopamine.

by analyzing the cathodic-to-anodic peak ratio of the CVs. If the pores trap FC^+, the cathodic current (FC^+ to FC), and consequently the cathodic-to-anodic peak ratio, should be greater for the Au-MSF electrodes than for Au electrodes. To investigate this, we analyzed the cathodic-to-anodic peak ratio of CVs recorded at three scan rates for 500 μM FC. At each scan rate, CVs normalized to their respective peak anodic current (Fc to FC^+) show an increase in the cathodic current after MSF deposition (Figures 6A-C). The original, non-normalized CVs are provided in Figure S8. Normalized CVs were used to better visualize the change in cathodic current, as the absolute current values can be influenced by MSF coverage. Statistical analysis further confirms that Au-MSF electrodes have greater cathodic-to-anodic peak ratios than their Au counterparts (Figures 6D-F). Additionally, the cathodic-to-anodic peak ratio increases at higher scan rates for Au-MSF electrodes, a trend previously reported for other trapping systems.[34] This is likely due to the oxidized species having less time to diffuse out of the pores, leading to further FC^+ accumulation. Comparisons between Au(G)-MSF and Au(UG)-MSF electrodes showed no statistically significant difference at 0.05 and 0.10 V/s (Figures 6D, E). Since most experiments were performed at 0.10 V/s, we conclude that the two electrode types perform similarly and can be chosen based on specific aims. Finally, it should be noted that the electrochemical signal changes much less than the plasmonic signal (Figures 2-4), which is likely the result of the greater sensitivity of PEM to local concentration changes, such as within the pores.[12]

We further investigated the effect of the negative charge of the MSF walls by experimentally adjusting the pH of the analyte solution. Since the isoelectric point of silica is known to

https://doi.org/10.1021/acselectrochem.4c00227
ACS Electrochem. 2025, 1, 974–986

be approximately pH 2, changing the pH of the solution can modify the MSF surface charge density, thereby influencing the enrichment of charged redox species.[31,37,38] As expected, at pH values at or below the isoelectric point of silica, there is a slight decrease in the peak cathodic current (Figure 7A) and a significant decrease in the dPEM/dt signal (Figure 7B). This is likely due to FC^+ no longer electrostatically adsorbing to the pore walls. Interestingly, there is minimal difference in the signals for solution pHs of 1.2 and 2.2 (corresponding to positively charged and neutral films, respectively), which may be due to similarities in the favorability of the oxidation reaction. Overall, the results support a model where the MSF modification increases the plasmonic signal due to the local enhancement of FC^+ cations, caused by their electrostatic attraction to the pore walls. Furthermore, the ability to tune the surface charge density of MSFs shows the potential of applying this setup to a wide array of charged species.

Imaging the Local Delivery of Dopamine. We next aimed to image locally delivered dopamine (DA). DA is a neurotransmitter with important roles in mood, cognition, memory, movement, and other fundamental processes.[39,40] Previous works have shown that the positive charge of dopamine at neutral and physiological pH allows for its selective detection in the presence of a negatively charged modification of the electrode surface.[41] Thus, the negatively charged MSF will theoretically induce a similar enhancement effect with DA as that with FC^+. Bulk detection experiments with DA yielded promising results: a Au-MSF electrode displayed greater sensitivity than a Au electrode for the oxidation of increasing concentrations of dopamine using CV (Figures S9A and S9B). This motivated us to utilize this new setup to detect the localized delivery of DA, mimicking the neurotransmitter release process in living systems.

Specifically, a micromanipulator system was employed to precisely control a 10 μm diameter dopamine-filled micropipette to generate a localized concentration gradient on the sensor surface (Figure 8A). Figures 8B−H shows the dPEM/dt signal distribution across the sensor surface during the anodic trace of a cyclic voltammogram recorded with the micropipette positioned approximately 3 μm above the sensor. Near 0.2 V, signal from the oxidation of DA appeared, peaking at 0.4 V. This is further corroborated by the extracted dPEM/dt signal plotted versus the voltage (Figure 8I) as well as a horizontal profile of the dPEM/dt signal at 0.4 V (Figure 8J) comparing the pipette area (red) to the background (black). Notably, DA preconcentration through a waiting period at −0.2 V was necessary, given that the extracted raw PEM signal for the delivery site shows a signal different from the background only in the first cycle, directly after the 20 s wait time (Figures S9C and S9D). This is likely due to the time required for DA adsorption onto the MSF walls, enabling effective nanoconfinement. Observing this behavior allowed us to subtract the second cycle to enhance the observed signal. It should be noted that the detected delivery site is not perfectly circular as in previous work.[42] This is a result of the dPEM/dt signal in this experiment being dependent on DA accumulation after nanoconfinement, which is highly sensitive to the heterogeneities of the electrode surface.

Although the micropipette was initially filled with 10 mM dopamine, mass transfer in the bulk solution caused the concentration at the orifice to decrease before approaching the sensor (Figure S9E). Numerical simulations indicate that the approximate concentration delivered to the sensor surface was no more than 1.5 mM (Figures S9F−H). Although this concentration remains at the millimolar level, the aim of this first trial was to demonstrate the microscopy capabilities of our new imaging setup with enhanced sensitivity enabled by MSF-generated nanoconfinement. Future work will aim to further improve the sensitivity of DA detection by adjusting parameters of the MSF and exploring the incorporation of catalytic nanoparticles or dopamine polymerization.[43−45]

Another focus of future work will be developing an accurate method for quantifying the concentrations, including both the source concentration (i.e., the concentration of redox species inside a delivery pipette or a sample of interest) and the surface concentration (i.e., the local concentration of redox species reaching the electrode surface). We have attempted two calibration approaches: the first involved exposing the system to bulk solutions with varying DA concentrations that approximately mimic the surface concentration, while the second used delivery pipettes filled with varying DA source concentrations. Both calibration curves exhibit linear dependence on their corresponding concentrations (Figure S10). However, both approaches have limitations, as discussed in the supporting information. At this stage, we consider them as proof-of-concept demonstrations, confirming the system's sensitivity to concentration changes. Further refinements will be required once a better sensitivity level is achieved.

Comparing Gridded and Ungridded Gold Electrodes. Although we have previously reported utilizing gridded gold electrodes for PEM measurements,[46] the use of ungridded gold electrodes is far more common. This work represents the first extensive application of gridded gold electrodes in this context. It is therefore important to compare the advantages and limitations of gridded versus ungridded gold electrodes. As discussed, the primary benefit of gridded gold electrodes is their ability to label specific locations for analysis, enabling a consistent examination of the same sensing area across different instruments. For instance, an area analyzed by PEM can be further characterized by AFM to reveal morphological details. In the context of biosensing with cells on MSFs, labels can potentially correlate PEM results with fluorescence microscopy data that provide cell-related information. This is essential given the inherent heterogeneity of all systems. However, gridded electrodes contribute to the heterogeneity of the substrate by introducing areas elevated approximately 200 nm above the surface (Figure S11). Despite this, both the current and the PEM signal are highly consistent between gridded and ungridded electrodes. Moreover, since PEM is a spatially resolved technique, any interference induced by the grid can be mitigated by analyzing only the signal from uniform areas and averaging the obtained signal. Similarly, the impact of the grid can be minimized by decreasing the size of the labels. Overall, gridded gold electrodes allow for precise measurements, while also providing surface labels for additional testing.

CONCLUSIONS

MSF modification of the PEM setup has been shown to improve the plasmonic imaging of FC and DA. The observed increase in the signal is demonstrated to be a result of the nanoconfinement of FC^+ and DA to the negatively charged walls of the mesopores, thereby causing a greater refractive index change and a correspondingly greater PEM signal. Thanks to its spatial and temporal resolution, PEM provides information not otherwise accessible through traditional electrochemical methods. For instance, PEM enabled real-

https://doi.org/10.1021/acselectrochem.4c00227
ACS Electrochem. 2025, 1, 974−986

time visualization of the deposition process, providing valuable insights into the mechanism of MSF formation. By enhancing the PEM and dPEM/dt signals, MSF-enabled nanoconfinement significantly broadens the potential applications of PEM, facilitating the plasmonic detection of redox species at micromolar concentrations. The tunable surface charge density of the nanopores further extends this capability to various redox-active molecules. This development is especially promising for PEM-based studies of biological systems, as MSFs have demonstrated significant size selectivity, theoretically enabling exclusion of large entities (*e.g.*, cell vesicles) while allowing smaller chemicals, such as neurotransmitters, to diffuse through.[47] This selectivity can enhance the specificity of neurotransmitter detection during exocytosis by preventing vesicular fouling of the sensing surface—a challenge observed in SPR studies.[48] Furthermore, MSFs can also shield cells from the potentials applied during PEM experiments, minimizing signal fluctuations due to cell movement and possible effects on cell metabolism.

The use of gridded gold electrodes as labels allows for the characterization of the same location of a sample using multiple techniques, which is necessary due to the fundamental heterogeneity of all systems, including cells. Future work will focus on optimizing the signal enhancement, leveraging the observed enhanced DA detection capabilities, and developing accurate calibration methods to perform real-time imaging of neurotransmitter release from cells.

EXPERIMENTAL SECTION

Chemicals and Materials. Ethanol (anhydrous), hydrochloric acid (HCl, 36%), and potassium ferricyanide (99%) were purchased from Thermo Fisher Scientific (Waltham, MA, United States). 1,1-ferrocenedimethanol (FC, 97%) and (3-mercaptopropyl)trimethoxysilane (MPTMS, 95%) were purchased from Sigma-Aldrich (Burlington, MA, United States). Sodium nitrate ($NaNO_3$, 99%), dopamine hydrochloride (DA, 99%), and tetraethoxysilane (TEOS, 98%) were purchased from Alfa Aesar (Ward Hill, MA, United States). Cetyltrimethylammonium bromide (CTAB, 98%) was purchased from MP Biomedicals (Irvine, CA, United States). Aqueous solutions were prepared with double-deionized water (resistivity = 18.2 MΩ cm at 25 °C, Milli-Q Ultrapure water EQ 7000 Purification System, MilliporeSigma, Burlington, MA). All chemicals were used as received.

Ag/AgCl reference electrodes, Pt wire counter electrodes, and Au(UG) electrodes were purchased from Biosensing Instruments (Tempe, AZ). Au(UG) electrodes consisted of an approximately 50 nm layer of Au deposited on top of a 2 nm Ti layer on a flat glass coverslip. Au(G) electrodes were fabricated by depositing a 2 nm Cr layer and a 47 nm Au layer via an e-beam evaporator (PVD 75, Kurt J Lesker) on gridded glass coverslips (Bellco Glass, Inc. Vineland, NJ, United States), which were cleaned with acetone in an ultrasonic bath for 10 min and rinsed with water. Gold rod electrodes and alumina polishing powder were purchased from CH Instruments (Austin, TX, United States). Silicon wells were cut from flexiPERM slides purchased from Sarstedt (Germany).

Mesoporous Silica Film Deposition. Two types of Au electrodes (ungridded and gridded) were applied for deposition of the silica film following reported procedures.[32] Prior to deposition, Au electrodes were washed with ethanol, followed by water, three times. After hydrogen flame annealing, the electrodes were pretreated with MPTMS (0.1 mM in ethanol) for 1 min. MPTMS was removed by rinsing the electrodes with ethanol. The starting sol consisted of 100 mM tetraethoxysilane (TEOS), 32 mM cetyltrimethylammonium bromide (CTAB), and 0.1 M $NaNO_3$ in 20 mL of water and 20 mL of ethanol. Its pH was adjusted to 3 using HCl, and it was stirred for 2.5 h at room temperature. The deposition was performed via amperometry using a potentiostat (CHI760E; CH Instruments, Austin, TX). Typically, a potential of -1.2 V (vs 1 M Ag/AgCl) was applied for 10 s to the MPTMS-modified electrode unless otherwise stated. When using PEM for real-time monitoring of the deposition process, the potential was only applied for 5 s to limit image overexposure. Similarly, for the test on a silica/gold boundary, a potential of -0.8 V (vs 1 M Ag/AgCl) was applied for 5 s to generate a thinner boundary. This led to a smaller angle shift, allowing us to use the same PEM detection angle to compare signals from the coated and uncoated parts of the same electrode. Most depositions were carried out with the electrodes lying horizontally on the setup, except for the generation of a boundary, where the deposition was performed by partially immersing the MPTMS-modified Au electrode vertically within the deposition solution. Following deposition, the electrode was rinsed with an acidic wash solution composed of 50 mM $NaNO_3$, 40 mM CTAB, and 19.5 mM HCl in 10 mL water and 10 mL EtOH (unless otherwise specified), after which the electrode was rinsed with water. After drying overnight in an oven at 130 °C, the CTAB template was removed by immersing the film-coated electrode in a solution of 0.1 M HCl under mild stirring for 15 min. Alternatively, electrochemical testing was performed before surfactant removal. Deposition on gold rod electrodes was conducted similarly, with the exception that the electrodes were polished by using an alumina slurry solution prior to deposition.

Plasmonic Electrochemical Microscopy. Plasmonic images were recorded by coupling a surface plasmon resonance microscopy system (SPRM 200 Series; Biosensing Instruments, Tempe, AZ, United States) to an electrochemical cell connected to a potentiostat. The cell consists of a three-electrode system: a Au electrode serving as the working electrode with an attached silicon well (exposed area of 0.9 cm^2), a Pt counter electrode, and a Ag/AgCl reference electrode (1 M KCl). Throughout the deposition process, Au electrodes were characterized with cyclic voltammetry using FC before deposition, before surfactant removal, and after surfactant removal. For all figures, the first cycle cyclic voltammograms (CVs) are shown. PEM images were taken at 50 frames per second using the Image SPR 1.8 application (Biosensing Instruments, Tempe, AZ, United States) and recorded as image stacks, while real-time data from 88 ROIs (regions of interest, 54 μm × 54 μm) were simultaneously plotted and recorded as numeric data. Further details of the PEM procedure can be found in the Supporting Information. PEM signals were presented either with original intensities or their time derivative (dPEM/dt) in the format of image snapshots or graphs plotted against time or applied voltages. All plotted graphs and images are in percentage units (%) for PEM signals or percentage units per time (%/s) for dPEM/dt signals. The percent unit represents the absolute intensity divided by the 16-bit integer limit. Note that all plasmonic signals shown were not intended to be calibrated to match the local current density. All conclusions were made by comparing the relative plasmonic signals for each redox species. All graphs follow the US convention for plotting voltammetric curves,

https://doi.org/10.1021/acselectrochem.4c00227
ACS Electrochem. 2025, 1, 974−986

using a Au working electrode, a Pt counter electrode, and an Ag/AgCl (1 M KCl) reference electrode.

Micromanipulator Dopamine Delivery. For local delivery sensing experiments, dopamine was released to the Au(G)-MSF electrode using a micropipet controlled by a 3-Axis Micromanipulator System (TRIO/MP-245A, Sutter Instrument, Novato, CA, USA) and a head stage (Axon Instrument, CV 203BU Molecular Device, San Jose, CA, USA). Micropipettes with a tip diameter of approximately 10 μm were pulled from quartz capillaries (1.0 mm O.D., 0.5 mm i.d., 7.5 cm length) using a P-2000 laser puller (Sutter Instrument, Novato, CA, USA). The parameters were set to Heat = 600, Filament = 4, Velocity = 20, Delay = 120, and Pull = 45. The quartz micropipettes, filled with a 10 mM solution of dopamine, cautiously approached the electrode. Upon contact, denoted by a parabolic scattering pattern in the plasmonic image, the pipette was retracted to the desired height above the surface. The pipette was moved to a different region after contact to avoid interference from the scratched region of the sensing surface. While the collision may have slightly damaged the pipette, it does not compromise our experimental assumptions, as the pipette is used only as a localized source of DA. Cyclic voltammetry was then performed after amperometric pretreatment at -0.2 V for 20 s. The plotted graphs show the signal of the second cycle subtracted from that of the first cycle.

Statistical Comparison of Peak Ratio. Peak ratios of Au(G), Au(UG), Au(G)-MSF, and Au(UG)-MSF electrodes were compared by performing a student's t-test using IBM SPSS Statistics 27.0 (International Business Machines Corporation, Armonk, NY, United States).

Numerical Simulation Based on Finite-Element Method. Finite element method simulations of FC and DA diffusion were conducted in COMSOL Multiphysics 6.0 and 6.2, respectively, using the "transport of diluted species" and "electrostatics" modules. Detailed description of the simulations can be found in the supplementary document.

■ ASSOCIATED CONTENT

Supporting Information

The Supporting Information is available free of charge at https://pubs.acs.org/doi/10.1021/acselectrochem.4c00227.

Additional experimental and numerical simulation details, additional electrochemical, plasmonic, simulation, and atomic force microscopy data, and COMSOL model reports (PDF)

■ AUTHOR INFORMATION

Corresponding Authors

Chong Liu − *Department of Chemistry and Biochemistry, University of California, Los Angeles, Los Angeles, California 90095, United States;* orcid.org/0000-0001-5546-3852; Email: chongliu@chem.ucla.edu

Yixian Wang − *Department of Chemistry and Biochemistry, California State University, Los Angeles, Los Angeles, California 90032, United States;* orcid.org/0000-0001-8691-1128; Email: ywang184@calstatela.edu

Authors

Samuel Groysman − *Department of Chemistry and Biochemistry, California State University, Los Angeles, Los Angeles, California 90032, United States;* orcid.org/0009-0006-5008-6772

Yisi Chen − *Department of Chemistry and Biochemistry, University of California, Los Angeles, Los Angeles, California 90095, United States*

Adaly Garcia − *Department of Chemistry and Biochemistry, California State University, Los Angeles, Los Angeles, California 90032, United States*

Christian Martinez − *Department of Chemistry and Biochemistry, California State University, Los Angeles, Los Angeles, California 90032, United States*

Kevin Diego-Perez − *Department of Chemistry and Biochemistry, California State University, Los Angeles, Los Angeles, California 90032, United States*

Miriam Benavides − *Department of Chemistry and Biochemistry, California State University, Los Angeles, Los Angeles, California 90032, United States*

Yi Chen − *Department of Chemistry and Biochemistry, University of California, Los Angeles, Los Angeles, California 90095, United States;* orcid.org/0000-0002-6660-5198

Zijian Wan − *Biodesign Center for Biosensors and Bioelectronics, Arizona State University, Tempe, Arizona 85281, United States;* orcid.org/0000-0001-7923-6451

Shaopeng Wang − *Biodesign Center for Biosensors and Bioelectronics, Arizona State University, Tempe, Arizona 85281, United States; School of Biological and Health Systems Engineering, Arizona State University, Tempe, Arizona 85281, United States;* orcid.org/0000-0002-2680-0503

Rujia Liu − *School of Chemical Sciences, University of Chinese Academy of Sciences, Beijing 100049, P. R. China*

Dengchao Wang − *School of Chemical Sciences, University of Chinese Academy of Sciences, Beijing 100049, P. R. China;* orcid.org/0000-0002-4909-7830

Complete contact information is available at: https://pubs.acs.org/10.1021/acselectrochem.4c00227

Author Contributions

YW is credited with the conceptual design of the project. SG prepared the MSF samples with the advice of YC and MB. SG performed PEM experiments and carried out data analysis. KDP performed SEM characterization of the samples with the help of SG. AG and SG performed AFM characterization of the samples. YC and SG performed COMSOL simulations with the help of RL, DW, and CL. CM, AG, and SG performed micromanipulator experiments. ZW and SW fabricated the Au(G) electrodes. SG prepared the figures with the help of YW, CL, and YC. The manuscript was written through contributions of all authors. All authors have given approval to the final version of the manuscript.

Notes

The authors declare no competing financial interest.

■ ACKNOWLEDGMENTS

This work was supported by National Science Foundation (NSF) CAREER award (CHE-2045839, YW, AG, SG), NSF MRI (CHE-1828334, YW), and California State University Program for Education and Research in Biotechnology (CSUPERB) 2022 Presidents' Commission Scholars Grant (SG, YW). This work has also been partially supported by NSF PREM (DMR-1523588, MB), NSF CREST (HRD-2112554, KDP), the National Institutes of Health (Grant

T34GM145503, CM, R35GM138241, CL, and R01GM140193, SW), and the Natural Science Foundation of China (22374150, DW, RL). ZW and SW acknowledge the use of facilities within the Arizona State University NanoFab supported in part by NSF program NNCI-ECCS-1542160. The content is solely the responsibility of the authors and does not necessarily represent the official views of NSF and NIH.

REFERENCES

(1) Gerroll, B. H. R.; Kulesa, K. M.; Ault, C. A.; Baker, L. A. Legion: An Instrument for High-Throughput Electrochemistry. *ACS Meas. Sci. Au* **2023**, *3*, 371−379.
(2) Amemiya, S.; Bard, A. J.; Fan, F.-R. F.; Mirkin, M. V.; Unwin, P. R. Scanning Electrochemical Microscopy. *Annu. Rev. Anal. Chem.* **2008**, *1*, 95−131.
(3) Ebejer, N.; Güell, A. G.; Lai, S. C. S.; McKelvey, K.; Snowden, M. E.; Unwin, P. R. Scanning Electrochemical Cell Microscopy: A Versatile Technique for Nanoscale Electrochemistry and Functional Imaging. *Annu. Rev. Anal. Chem.* **2013**, *6*, 329−351.
(4) Bouffier, L.; Doneux, T. Coupling Electrochemistry with in Situ Fluorescence (Confocal) Microscopy. *Curr. Opin. Electrochem.* **2017**, *6*, 31−37.
(5) Moldovan, R.; Vereshchagina, E.; Milenko, K.; Iacob, B.-C.; Bodoki, A. E.; Falamas, A.; Tosa, N.; Muntean, C. M.; Farcău, C.; Bodoki, E. Review on Combining Surface-Enhanced Raman Spectroscopy and Electrochemistry for Analytical Applications. *Anal. Chim. Acta* **2022**, *1209*, 339250.
(6) Chieng, A.; Chiang, M.; Triloges, K.; Chang, M.; Wang, Y. Recent Progress in the Studies of Electrochemical Interfaces by Surface Plasmon Resonance Spectroscopy and Microscopy. *Curr. Opin. Electrochem.* **2019**, *13*, 94−99.
(7) Wang, Y.; Cao, Z.; Yang, Q.; Guo, W.; Su, B. Optical Methods for Studying Local Electrochemical Reactions with Spatial Resolution: A Critical Review. *Anal. Chim. Acta* **2019**, *1074*, 1−15.
(8) Shan, X.; Patel, U.; Wang, S.; Iglesias, R.; Tao, N. Imaging Local Electrochemical Current via Surface Plasmon Resonance. *Science* **2010**, *327*, 1363−1366.
(9) Yuan, T.; Wang, W. Studying the Electrochemistry of Single Nanoparticles with Surface Plasmon Resonance Microscopy. *Curr. Opin. Electrochem.* **2017**, *6*, 17−22.
(10) Sambur, J. B.; Chen, T.-Y.; Choudhary, E.; Chen, G.; Nissen, E. J.; Thomas, E. M.; Zou, N.; Chen, P. Sub-Particle Reaction and Photocurrent Mapping to Optimize Catalyst-Modified Photoanodes. *Nature* **2016**, *530*, 77−80.
(11) Huang, B.; Yu, F.; Zare, R. N. Surface Plasmon Resonance Imaging Using a High Numerical Aperture Microscope Objective. *Anal. Chem.* **2007**, *79*, 2979−2983.
(12) Zhou, X.; Yang, Y.; Wang, S.; Liu, X. Surface Plasmon Resonance Microscopy: From Single-Molecule Sensing to Single-Cell Imaging. *Angew. Chem. Int. Ed.* **2020**, *59*, 1776−1785.
(13) Shan, X.; Wang, S.; Wang, W.; Tao, N. Plasmonic-Based Imaging of Local Square Wave Voltammetry. *Anal. Chem.* **2011**, *83*, 7394−7399.
(14) Wang, Y.; Shan, X.; Cui, F.; Li, J.; Wang, S.; Tao, N. Electrochemical Reactions in Subfemtoliter-Droplets Studied with Plasmonics-Based Electrochemical Current Microscopy. *Anal. Chem.* **2015**, *87*, 494−498.
(15) Zhao, R.; Yan, B.; Li, D.; Guo, Z.; Huang, Y.; Wang, D.; Yao, X. An Ultramicroelectrode Electrochemistry and Surface Plasmon Resonance Coupling Method for Cell Exocytosis Study. *Anal. Chem.* **2024**, *96*, 10228.
(16) Zhang, B.; Adams, K. L.; Luber, S. J.; Eves, D. J.; Heien, M. L.; Ewing, A. G. Spatially and Temporally Resolved Single-Cell Exocytosis Utilizing Individually Addressable Carbon Microelectrode Arrays. *Anal. Chem.* **2008**, *80*, 1394−1400.
(17) Lin, Y.; Trouillon, R.; Svensson, M. I.; Keighron, J. D.; Cans, A.-S.; Ewing, A. G. Carbon-Ring Microelectrode Arrays for Electrochemical Imaging of Single Cell Exocytosis: Fabrication and Characterization. *Anal. Chem.* **2012**, *84*, 2949−2954.
(18) Sundaresan, V.; Bohn, P. W. Acid-Base Chemistry at the Single Ion Limit. *Chem. Sci.* **2020**, *11*, 10951−10958.
(19) Jia, J.; Kwon, S.-R.; Baek, S.; Sundaresan, V.; Cao, T.; Cutri, A. R.; Fu, K.; Roberts, B.; Shrout, J. D.; Bohn, P. W. Actively Controllable Solid-Phase Microextraction in a Hierarchically Organized Block Copolymer-Nanopore Electrode Array Sensor for Charge-Selective Detection of Bacterial Metabolites. *Anal. Chem.* **2021**, *93*, 14481−14488.
(20) Reitemeier, J.; Baek, S.; Bohn, P. W. Hydrophobic Gating and Spatial Confinement in Hierarchically Organized Block Copolymer-Nanopore Electrode Arrays for Electrochemical Biosensing of 4-Ethyl Phenol. *ACS Appl. Mater. Interfaces* **2023**, *15*, 39707−39715.
(21) Goux, A.; Etienne, M.; Aubert, E.; Lecomte, C.; Ghanbaja, J.; Walcarius, A. Oriented Mesoporous Silica Films Obtained by Electro-Assisted Self-Assembly (EASA). *Chem. Mater.* **2009**, *21*, 731−741.
(22) Lu, J.; Fan, Y.; Howard, M. D.; Vaughan, J. C.; Zhang, B. Single-Molecule Electrochemistry on a Porous Silica-Coated Electrode. *J. Am. Chem. Soc.* **2017**, *139*, 2964−2971.
(23) Scala-Benuzzi, M. L.; Fernández, S. N.; Giménez, G.; Ybarra, G.; Soler-Illia, G. J. A. A. Ordered Mesoporous Electrodes for Sensing Applications. *ACS Omega* **2023**, *8*, 24128−24152.
(24) Wang, J.; Vilà, N.; Walcarius, A. Redox-Active Vertically Aligned Mesoporous Silica Thin Films as Transparent Surfaces for Energy Storage Applications. *ACS Appl. Mater. Interfaces* **2020**, *12*, 24262−24270.
(25) Manzano, M.; Vallet-Regí, M. Mesoporous Silica Nanoparticles for Drug Delivery. *Adv. Funct. Mater.* **2020**, *30*, 1902634.
(26) Oh, S.; Moon, J.; Kang, T.; Hong, S.; Yi, J. Enhancement of Surface Plasmon Resonance (SPR) Signals Using Organic Functionalized Mesoporous Silica on a Gold Film. *Sens. Actuators B Chem.* **2006**, *114*, 1096−1099.
(27) Li, J.; Lu, D.; Zhang, Z.; Liu, Q.; Qi, Z. Hierarchical Mesoporous Silica Film Modified near Infrared SPR Sensor with High Sensitivities to Small and Large Molecules. *Sens. Actuators B Chem.* **2014**, *203*, 690−696.
(28) Etienne, M.; Quach, A.; Grosso, D.; Nicole, L.; Sanchez, C.; Walcarius, A. Molecular Transport into Mesostructured Silica Thin Films: Electrochemical Monitoring and Comparison between *p* 6 *m*, P6 $_3$ / *Mmc*, and *Pm* 3 *n* Structures. *Chem. Mater.* **2007**, *19*, 844−856.
(29) Wang, G.; Wang, C.; Sun, S. An Optical Waveguide Sensor Based on Mesoporous Silica Films with a Comparison to Surface Plasmon Resonance Sensors. *Sens. Actuators B Chem.* **2018**, *255*, 3400−3408.
(30) Karman, C.; Vilà, N.; Walcarius, A. Amplified Charge Transfer for Anionic Redox Probes through Oriented Mesoporous Silica Thin Films. *ChemElectroChem.* **2016**, *3*, 2130−2137.
(31) Nasir, T.; Herzog, G.; Hébrant, M.; Despas, C.; Liu, L.; Walcarius, A. Mesoporous Silica Thin Films for Improved Electrochemical Detection of Paraquat. *ACS Sens.* **2018**, *3*, 484−493.
(32) Ullah, W.; Herzog, G.; Vilà, N.; Brites Helú, M.; Walcarius, A. Electrochemically Assisted Deposition of Nanoporous Silica Membranes on Gold Electrodes: Effect of 3-Mercaptopropyl-(Trimethoxysilane) "Molecular Glue" on Film Formation, Permeability and Metal Underpotential Deposition. *ChemElectroChem.* **2021**, *8*, 142−150.
(33) Walcarius, A. Electroinduced Surfactant Self-Assembly Driven to Vertical Growth of Oriented Mesoporous Films. *Acc. Chem. Res.* **2021**, *54*, 3563−3575.
(34) Shao, Z.; Chang, Y.; Venton, B. J. Carbon Microelectrodes with Customized Shapes for Neurotransmitter Detection: A Review. *Anal. Chim. Acta* **2022**, *1223*, 340165.
(35) Wang, M.; Revil, A. Electrochemical Charge of Silica Surfaces at High Ionic Strength in Narrow Channels. *J. Colloid Interface Sci.* **2010**, *343*, 381−386.
(36) Schoch, R. B.; Han, J.; Renaud, P. Transport Phenomena in Nanofluidics. *Rev. Mod. Phys.* **2008**, *80*, 839−883.

https://doi.org/10.1021/acselectrochem.4c00227
ACS Electrochem. 2025, 1, 974−986

(37) Vilà, N.; De Oliveira, P.; Walcarius, A.; Mbomekallé, I. M. pH-Modulated Ion Transport and Amplified Redox Response of Keggin-Type Polyoxometalates through Vertically-Oriented Mesoporous Silica Nanochannels. *Electrochimica Acta* **2019**, *309*, 209−218.
(38) Fattakhova-Rohlfing, D.; Wark, M.; Rathouský, J. Ion-Permselective pH-Switchable Mesoporous Silica Thin Layers. *Chem. Mater.* **2007**, *19*, 1640−1647.
(39) Diehl, D. J.; Gershon, S. The Role of Dopamine in Mood Disorders. *Compr. Psychiatry* **1992**, *33*, 115−120.
(40) Nieoullon, A. Dopamine and the Regulation of Cognition and Attention. *Prog. Neurobiol.* **2002**, *67*, 53−83.
(41) Promsuwan, K.; Soleh, A.; Saisahas, K.; Saichanapan, J.; Kanatharana, P.; Thavarungkul, P.; Guo, C.; Li, C. M.; Limbut, W. Discrimination of Dopamine by an Electrode Modified with Negatively Charged Manganese Dioxide Nanoparticles Decorated on a Poly(3,4 Ethylenedioxythiophene)/Reduced Graphene Oxide Composite. *J. Colloid Interface Sci.* **2021**, *597*, 314−324.
(42) Garcia, A.; Dhoj, C.; Groysman, S.; Wang, K.; Ao, S.; Anguiano, A.; Tran, T.; Jiang, D.; Wang, Y. Prussian Blue Nanofilm-Sensitized Plasmonic Electrochemical Microscopy for Spatially Resolved Detection of the Localized Delivery of Hydrogen Peroxide. *Sens. Actuators Rep.* **2024**, *8*, 100218.
(43) Zhao, R.; Li, D.; Yin, N.; Guo, Z.; Wang, D.; Yao, X. The High Sensitive and Selective Detection of Dopamine Based on Its Electropolymerization by Electrochemical Surface Plasmon Resonance. *Sens. Actuators B Chem.* **2022**, *370*, 132401.
(44) Nasir, T.; Shao, L.; Han, Y.; Beanland, R.; Bartlett, P. N.; Hector, A. L. Mesoporous Silica Films as Hard Templates for Electrodeposition of Nanostructured Gold. *Nanoscale Adv.* **2022**, *4*, 4798−4808.
(45) Yusoff, N.; Pandikumar, A.; Ramaraj, R.; Lim, H. N.; Huang, N. M. Gold Nanoparticle Based Optical and Electrochemical Sensing of Dopamine. *Microchim. Acta* **2015**, *182*, 2091−2114.
(46) Garcia, A.; Wang, K.; Bedier, F.; Benavides, M.; Wan, Z.; Wang, S.; Wang, Y. Plasmonic Imaging of Electrochemical Reactions at Individual Prussian Blue Nanoparticles. *Front. Chem.* **2021**, *9*, 718666.
(47) Vilà, N.; André, E.; Ciganda, R.; Ruiz, J.; Astruc, D.; Walcarius, A. Molecular Sieving with Vertically Aligned Mesoporous Silica Films and Electronic Wiring through Isolating Nanochannels. *Chem. Mater.* **2016**, *28*, 2511−2514.
(48) Moreira, B.; Tuoriniemi, J.; Kouchak Pour, N.; Mihalčíková, L.; Safina, G. Surface Plasmon Resonance for Measuring Exocytosis from Populations of PC12 Cells: Mechanisms of Signal Formation and Assessment of Analytical Capabilities. *Anal. Chem.* **2017**, *89*, 3069−3077.

https://doi.org/10.1021/acselectrochem.4c00227
ACS Electrochem. 2025, 1, 974−986